Solar Energy Materials & Solar Cells 288 (2025) 113615

Contents lists available at ScienceDirect

Solar Energy Materials and Solar Cells

journal homepage: www.elsevier.com/locate/solmat

Enhancing composite phase change material thermal performance by tuning phase change materials properties with nanoparticles

A. Anagnostopoulos [a,b,*], M. Elena Navarro [a,**], Zhu Jiang [c], Yulong Ding [a,***]

[a] Birmingham Centre for Energy Storage & School of Chemical Engineering, University of Birmingham, Birmingham, B15 2TT, United Kingdom
[b] Institute of Chemistry, University of Silesia, Szkolna 9, 40-006, Katowice, Poland
[c] School of Energy & Environment, Southeast University, Nanjing, 210096, China

ARTICLE INFO

Keywords:
Thermal energy storage
Composite phase change materials
Nanoparticles
Waste heat recovery
Fly ash
High-temperature

ABSTRACT

Thermal Energy Storage (TES) , particularly latent heat TES, is a promising solution for waste heat recovery. However, phase change materials (PCMs), the main TES media in LHTES systems, face challenges such as limited thermal conductivity and large volume changes during phase transitions. Encapsulating PCMs within porous matrices to fabricate Composite Phase Change Materials (CPCMs) can address these issues, though CPCMs are attained through expensive and/or complex processes and/or have relatively low PCM content. This study introduces the use of SiO_2 nanoparticles to enhance CPCMs, enabling the fabrication of CPCMs with high PCM content over 72 % through a simple mix sintering approach. The incorporation of nanoparticles enhances structural integrity and thermal performance. A CPCM, with 72 % $NaNO_3$ content, achieves structural integrity, surpassing the 60 % PCM limit typically achieved without nanoparticles. The sample showcases only a 14 % decrease in energy storage density compared to pure $NaNO_3$ with a 28 % increase in thermal conductivity and a much lower coefficient of thermal expansion compared to the PCM. Further research in this area can potentially resolve the current material level issues of latent heat TES.

1. Introduction

Heavy industries account for 27 % of total energy use and 30 % of CO_2 emissions in the EU [1,2]. Heating processes dominate their energy consumption, generating substantial waste heat, a large part of which (400 TWh/year) is available for recovery and reuse [3,4]. Thermal Energy Storage (TES) is a promising solution for industrial waste heat recovery (WHR), offering the ability to store and reuse energy to address demand/supply mismatches [5]. Unlike conventional methods like recuperators, TES reduces energy losses during intermittent operations and startup, making it more cost-effective and efficient [6].

TES systems are categorized into sensible, latent, and thermochemical storage. Among these, Latent Heat TES (LHTES) is the most promising and market-ready, offering high energy density and minimal temperature variation during operation, unlike the lower-density Sensible TES or the developmental-stage Thermochemical TES [7]. LHTES, utilizing phase change materials (PCMs), It has been widely applied in WHR, solar energy capture, and grid management [8]. However, PCMs face challenges such as low thermal conductivity, corrosion, volume changes during phase transitions, and subcooling, which limit their effectiveness in LHTES [9]. Integrating PCMs into porous matrices forms Composite Phase Change Materials (CPCMs), which address these issues by enhancing physicochemical stability, thermal conductivity, and structural integrity[10–14]. While CPCMs trade off some energy storage efficiency, they excel in heat transfer and durability. Moreover, CPCMs play a critical role in hybrid TES systems, which combine latent and sensible heat storage for highly efficient energy recovery [15].

CPCM fabrication methods include melting infiltration, mix sintering, and sol-gel processes. Among these, mix sintering stands out as the most practical for mass production due to its simplicity and scalability compared to the other two [9,16].This method involves compacting PCM particles with a supportive material, followed by sintering, and has been successfully demonstrated at the pilot scale [17].

Structural stability is the biggest challenge in CPCM development,

* Corresponding author. Birmingham Centre for Energy Storage & School of Chemical Engineering, University of Birmingham, Birmingham, B15 2TT, United Kingdom.
** Corresponding author.
*** Corresponding author.
E-mail addresses: a.anagnostopoulos@bham.ac.uk (A. Anagnostopoulos), h.navarro@bham.ac.uk (M.E. Navarro), y.ding@bham.ac.uk (Y. Ding).

https://doi.org/10.1016/j.solmat.2025.113615
Received 14 January 2025; Received in revised form 24 February 2025; Accepted 27 March 2025
Available online 11 April 2025
0927-0248/© 2025 The Authors. Published by Elsevier B.V. This is an open access article under the CC BY license (http://creativecommons.org/licenses/by/4.0/).

particularly at higher PCM concentrations. Problems like leakage and deformation arise due to several factors, including volume changes during PCM phase transitions, viscosity, and poor wetting dynamics between the PCM and matrix. In mix sintering, three distinct scenarios emerge. First, if pore volume is sufficient, the PCM transitions without structural issues (usually at low PCM content). Second, insufficient pore volume causes overpressure during PCM expansion, leading to swelling, cracking, or matrix collapse. Third, the PCM moves freely within the porous network and can form a stable structure, but poor wetting and/or oversized pores lead to increased leakage [18]. These factors limit PCM content in oxide-based CPCMs to approximately 60 %, even with systematic efforts to minimize porosity and maximize accommodation through matrix tuning [9].

The 60 % PCM content threshold in CPCMs is well-documented. Sang et al. reported a 50 wt% limit in carbonate salt-MgO composites [19], while Xu et al. observed a 60 % limit in $NaNO_3$-Diatomite CPCMs, despite diatomite's high surface area and small particle size [20]. Miliozzi et al. found that exceeding 60 % PCM in diatomite-$NaNO_3$ CPCMs led to inhomogeneous mixtures [21], a trend also seen in $NaNO_3/SiO_2$ CPCMs [22]as well as alternative matrices like red mud, waste foundry sand [23,24], recycled blast furnace slag [25] and dolomite [26]. Majority of attempts to exceed the 60 % threshold have focused on enhancing matrix porosity through treatments like calcination and chemical modification [27]. However, even with such improvements, studies continue to report the same 60 % limit [28].

Recent studies have explored nanoparticle (NP) doping to enhance CPCM stability and thermal performance. For instance, Yu et al. incorporated SiO_2 nanoparticles into an expanded graphite (EG) CPCM based on Solar Salt ($NaNO_3$-KNO_3), identifying an optimal SiO_2 nanoparticle concentration of 1 wt% for boosting thermal conductivity and specific heat capacity [29]. In another study, Guo et al. [30] improved the stability and thermal properties of a Na_2CO_3-K_2CO_3/MgO CPCM through SiO_2 nanoparticle doping. Ye et al. achieved comparable enhancements by integrating multi-walled carbon nanotubes (MWCNTs) into a Na_2CO_3/MgO CPCM [31]. Additionally, Feng et al. discovered that doping diatomite-$NaNO_3$ CPCMs with SiC nanoparticles could elevate the conductivity by up to 265 % [32]. Luo et al. further expanded on these findings by embedding $LiNO_3$/NaCl eutectics within a three-dimensional (3D) hierarchical ultralight silicon carbide (SiC) foam, doping it with 1 % SiO_2 nanoparticles. This modification resulted in a significant increase in thermal conductivity (159 %) and a slight enhancement in specific heat capacity (4.86 %) when compared to the unaltered molten PCM [33]. Song et al. developed stable $NaNO_3$/NP/EG composites using a mechanical dispersion method, blending sodium nitrate with specific nanoparticles (1 wt% SiO_2, 0.9 wt% TiO_2 + 0.1 wt% SiO_2) and varying EG concentrations [34] They found that at 15 wt% EG, the composites achieved excellent chemical compatibility, structural integrity, and significantly enhanced thermal properties without sacrificing thermal stability over numerous heating-cooling cycles. Yu et al. crafted a novel high-temperature thermal storage composite, merging eutectic chloride ($MgCl_2$–NaCl–KCl) with EG and 1 wt % SiO_2 NPs [35]. This resulting material enhanced thermal properties and leakage prevention. Notably, SiO_2 NPs significantly increase the CPCM's specific heat and thermal conductivity. Kang et al. designed a CPCM consisting of a molten salt (NaF-Na_2CO_3-Na_2SO_4)-EG-graphene nanoplatelets, achieving over 1100 % improvement in thermal conductivity [36].

A common aspect of the studies discussed above is the simultaneous mixing of nanoparticles, PCM, and matrix material. While this method enhances thermal properties, it also introduces significant structural challenges. Increasing nanoparticle content in these systems often leads to defects within the solid matrix, amplifying porosity and weakening the structure [25]. This results in leakage, deformation, and breakage [25]. This effectively limits the potential of these approaches to PCM contents of ~60 %.

In stark contrast to these methods, a stepwise incorporation strategy is proposed. Here, NPs are first pre-mixed with the PCM to formulate a nano-enhanced PCM, which is then combined with the matrix. This method leverages the well-documented ability of NPs to improve not only the thermal properties of the PCM but also its viscosity [37], coefficient of thermal expansion [38], surface tension [39], and wettability [39]. Higher viscosity reduces PCM movement, minimizing internal stress in the CPCM. Enhanced surface tension improves grain cohesion and structural compactness, while better wettability reduces leakage.

For the first time, this stepwise approach allows us to surpass the traditional 60 % PCM content threshold, achieving stability at PCM contents exceeding 70 % using a simple and scalable mix sintering protocol. Unlike more complex methods such as etching, vacuum infiltration, or sol-gel processing, this straightforward approach paves the way for practical, cost-effective CPCM fabrication with superior thermal performance and structural stability.

2. Materials and methods

2.1. Materials

Sodium nitrate ($NaNO_3$) was used as the PCM, modified with amorphous silica NPs (SiO_2, 10 nm, >99 % purity, Sigma Aldrich). Following a variation of the method by Sidik et al. [40], SiO_2 NPs were first dispersed in deionized water via ultrasonication (90 min) to ensure uniformity. $NaNO_3$ was then added and further sonicated for 180 min before drying at 150 °C to remove residual water (Fig. 1).

Fly ash (FA), sourced from the Ptolemais thermal power station in Western Macedonia, Greece [37], was used as the matrix material. FA is classified as a fine-grained material, with more than 85 % of its particles smaller than 0.075 mm and a mean particle size (d_{50}) of 23.3 μm [41]. It contains a majority of silt-sized spherical particles (79 % by weight), and its relatively high surface area and hydraulic properties contribute positively to the structural stability of CPCMs. It is primarily composed of SiO_2 (31.3 %), CaO (32.9 %), and Al_2O_3 (12.3 %), among other oxides (Table 1) [41]. As a major industrial byproduct of coal combustion, over half a billion tons of FA are produced annually, with only 25–35 % repurposed [38]. While typically used in construction, its high thermal stability and density make it a promising alternative for CPCMs.

CPCMs were prepared by milling and mixing the FA with the NP-PCM mixture, followed by compression molding at 20 MPa for 1 min to form 13 mm diameter cylindrical pellets. Samples for thermal cycling were molded to ~20 mm height, while those for Laser Flash Analysis (LFA) were compressed to <2 mm. The pellets were then sintered at 450 °C for 3 h, ensuring matrix integration and the formation of a cohesive nano-enhanced CPCM (Fig. 2).

The results presented in Fig. 3 clearly demonstrate the stabilizing benefits of incorporating NPs into CPCMs. Motivated by these findings, the investigation was extended to CPCMs with a higher PCM content. This study aimed to determine how increasing NP levels impact structural integrity across different PCM compositions. To efficiently evaluate this, the NP (SiO_2) content was systematically varied from 5 to 10 wt% (Table 2).

It's evident that the addition of NPs generally enhances structural stability. However, the effectiveness of SiO_2 NPs in maintaining this stability diminishes as the $NaNO_3$ content increases. For instance, while adding just 1 wt % SiO_2 is adequate for stabilizing composites with 60 wt % $NaNO_3$, those containing 70 wt % $NaNO_3$ require a minimum of 5 wt % SiO_2 to remain coherent. Moreover, at 72 wt % $NaNO_3$, even a 5 wt % SiO_2 is insufficient to sustain structural integrity, indicating a limit to the effectiveness of NPs at very high PCM concentrations.

Nevertheless, the ability to push FA-based CPCMs to accommodate up to 72 % $NaNO_3$ represents a significant leap forward, particularly when considering that such compositions were previously unstable even at 60 wt% PCM content.

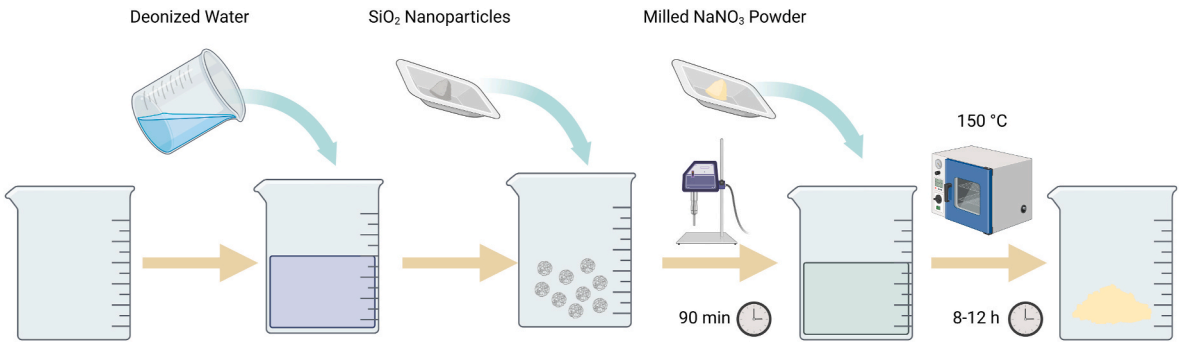


Fig. 1. Step-by-step preparation of $NaNO_3$-SiO_2 nanoparticle mixtures. Preparation steps of $NaNO_3$-SiO_2 nanoparticle composites, from initial mixing to final drying.

Table 1
Composition of the fly ash utilized as part of this investigation [41].

Element	SiO_2	Al_2O_3	Fe_2O_3	CaO	MgO	Na_2O	K_2O	SO_3	TiO_2	IL	Cl-
Percentage	31.3	12.3	5.5	32.9	3.1	0.52	1.3	5.9	0.7	5.4	1.8

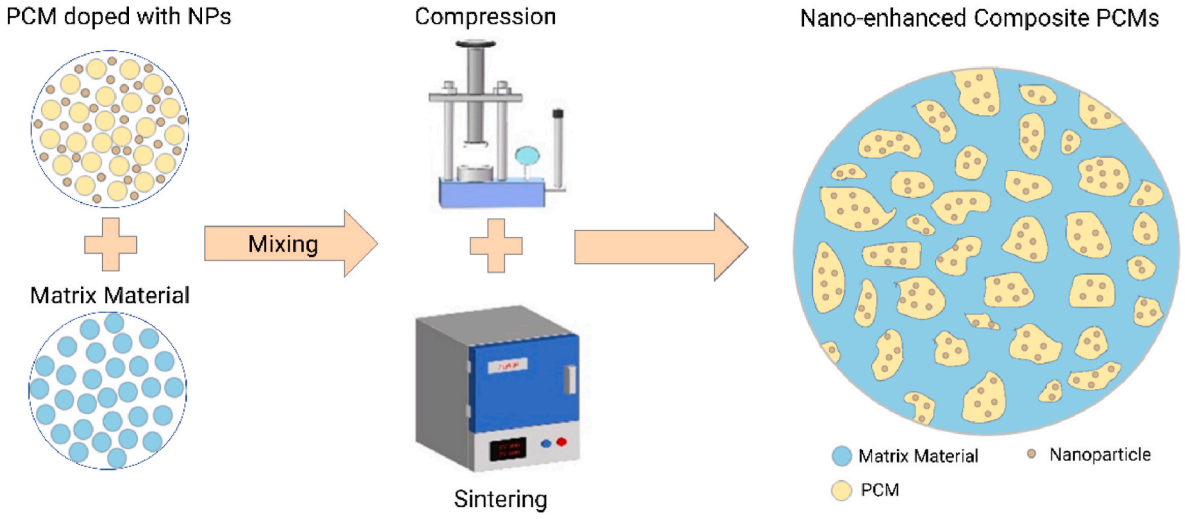


Fig. 2. Production stages of composite PCMs, detailing material incorporation, compression molding, and sintering to achieve the final nano-enhanced structure.

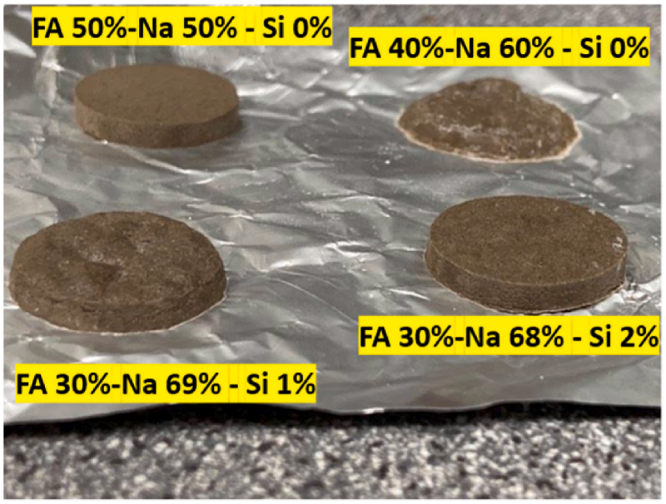


Fig. 3. Pellets of FA and sodium nitrate (Na) composites with varying Si nanoparticle (NP) percentages, demonstrating material stability after thermal processing.

2.2. Methods

X-Ray Diffraction (XRD) analysis was performed using a Bruker D8 Advance system, with a scan rate of 2° per minute at ambient temperature in an atmospheric environment.

For the thermal analysis, Differential Scanning Calorimetry (DSC) was employed utilizing a Mettler Toledo DSC3 instrument. These measurements were executed at a rate of 5 °C per minute heating rate under atmospheric conditions, in compliance with DIN51007 standards, using the sapphire calibration method.

The thermal diffusivity was evaluated using the Laser Flash Analysis (LFA) method on a Netzsch LFA 427 apparatus. Samples were prepared with a surface coating of graphite to ensure accurate measurements. Thermal conductivity was then deduced from the following equation:

$$k = a\rho C_p \tag{1}$$

where k represents thermal conductivity (W/mK), a is thermal diffusivity (mm^2/s), ρ denotes density (g/cm^3), and C_p is the specific heat capacity (J/gK).

Thermal expansion coefficients were determined using an optical dilatometer, specifically the TA Instrument DILA-806, over a temperature range from room temperature to 500 °C. Pellet samples, roughly 13

Table 2
Stability assessment of CPCMs containing varying percentages of fly ash (FA), sodium nitrate (Na), and silicon dioxide (SiO_2) NPs.

Sample Name	Fly Ash (%)	$NaNO_3$ (%)	SiO_2 (wt. %)	Result
F40N60Si0	40	60.0	0.0	
F40N59Si06	40	59.4	0.6	
F40N57Si3	40	57	3	
F40N54Si6	40	54	6	
F30N69Si07	30	69.3	0.7	
F30N66Si35	30	66.5	3.5	
F30N63Si7	30	63	7	
F20N79Si08	20	79.2	0.8	
F20N76Si4	20	76	4	
F20N72Si8	20	72	8	

mm in diameter, underwent a controlled heating regime of 5 K/min in an air atmosphere.

For the microstructure and elemental distribution, Scanning Electron Microscopy (SEM) analyses were conducted on a JEOL JSM-7001F instrument, integrated with an Energy-Dispersive X-ray Spectroscopy (EDX) system, Quantax 70 from Bruker, equipped with an XFlash® 430H detector. EDX analysis allows for the identification and mapping of elements between boron and americium (atomic numbers 5 to 95), through the emission of characteristic X-rays corresponding to each element's unique electronic structure.

Thermal cycling tests were carried out using a dilatometer from TA Instruments, setting the temperature fluctuations between 230 °C and 400 °C, with a 20-min isothermal hold at both the peak and trough temperatures.

Density measurements were taken with a helium pycnometer, the Accupyc II 1340 from Micromeritics.

Additionally, X-Ray nano-Computed Tomography (nano-CT) was utilized for assessing microstructural properties and pore distribution using a Skyscan 2211 system. Cylinder samples of dimensions φ 2 × 15 mm were examined under a voltage of 95 kV and a current of 150 μA, capturing projection images at 0.1° increments over a 180° rotation, achieving a pixel resolution of 9.5 μm. Three-dimensional reconstruction of the scanned samples was processed using Recon software, and the resultant 3D structures were analyzed and visualized with CTan software.

3. Results and discussion

3.1. Chemical composition and thermal stability

3.1.1. X-ray diffraction (chemical stability)

The XRD analysis of the thermally cycled CPCMs highlights the resilience of the chemical structure post-cycling (Fig. 4).

The pure $NaNO_3$ displayed sharp, well-defined peaks, consistent with its highly ordered crystal structure. In contrast, the FA sample showed broader peaks, indicating a more amorphous or less ordered state, which is reflected in its heterogeneous composition (Table 1).

When compared to the pure FA pattern, the composite FA40NA50Si5 shows a significant modification in the peak profile (Fig. 4a). Some of the peaks initially present in the FA have either diminished or disappeared in the composite. The first missing peak at 26° is typically associated with anhydrite, a calcium sulfate mineral that is often observed in high-calcium FA samples such as the one used in this study [42]. Its absence in the composite may suggest alterations due to the sintering process or a dilution effect where its crystalline signal is subdued by the presence of the more dominant $NaNO_3$ and SiO_2 phases.

The second and third absent peaks, found at 37° and 54°, are related to lime (CaO) [42], a component that has been reported in the literature to become disordered at elevated temperatures [43]. Given the sintering temperature of 500 °C employed in this study, it is plausible that the heat contributed to the disordering of the lime's crystalline structure, resulting in a reduction or disappearance of these peaks. This alteration is likely accentuated by the FA's generally more inhomogeneous structure and the mixing with $NaNO_3$ and amorphous SiO_2 nanoparticles, which could contribute to further disruption of the crystal order, leading to the weakening or vanishing of these FA-related peaks.

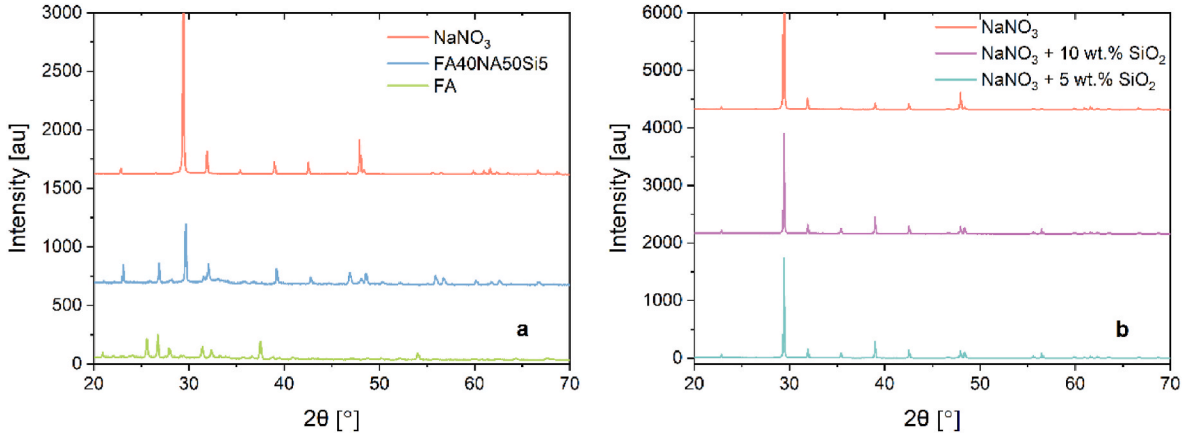


Fig. 4. (a) XRD patterns of pure fly ash (FA), $NaNO_3$, and the FA40NA50Si5 composite, (b) XRD comparison of pure $NaNO_3$ with $NaNO_3$ containing 5 wt% and 10 wt % SiO_2 nanoparticles.

Nevertheless, the characteristic peaks of $NaNO_3$ are evidently present in the composite, indicating that its crystalline structure remains intact, which supports the hypothesis that the interaction between $NaNO_3$ and the FA is purely physical and not chemical. These peaks could not be attributed to the SiO_2 NPs, as they are amorphous and do not contribute to the XRD pattern in this manner.

This conclusion is further substantiated by thermal analysis. The latent heat of the CPCM remains within the range of values predicted by the mixing theory, signifying that the properties of $NaNO_3$ are preserved post-composite formation.

The XRD patterns presented for $NaNO_3$ with 5 wt% and 10 wt% SiO_2 display a preserved crystalline structure of the sodium nitrate (Fig. 4b). Notably, the introduction of SiO_2 NPs does not lead to any discernible shift in most peaks' positions, confirming that the crystal structure of $NaNO_3$ remains largely unaffected by the presence of SiO_2. However, alterations in peak intensities are observed; a peak close to 47° exhibits a reduction in intensity, whereas adjacent peaks at 38° and 48° show an increase. These variations could indicate localized changes in the microstructure, potentially due to the distribution of SiO_2 nanoparticles within the salt.

One potential explanation for these intensity changes is the influence of SiO_2 NPs on diffraction conditions. The addition of amorphous NPs may introduce strains or slight lattice distortions in the $NaNO_3$ crystal, affecting X-ray diffraction and altering peak intensities [44]. For example, the peak at 38° is accentuated because the NPs act as nucleation sites, enhancing crystallinity, while the reduction at 47° could indicate areas where the NPs disrupt the crystal structure. The increased intensity at 48° may suggest constructive interference caused by the NPs.

3.1.2. Density/porosity (thermal-structural stability)

Evaluating the behavior of CPCMs after thermal cycling is crucial for assessing their long-term suitability in TES applications (Fig. 5). The data on density changes across various composite formulations before and after 100 thermal cycles reveals an intriguing pattern. Notably, there is a trend of reduced density that correlates with higher SiO_2 NP content. This decrease in density might be indicative of the physical behavior of the NPs within the matrix during cycling. Their addition of NPs might inhibit the rearrangement of particles during thermal cycling, leading to a less dense arrangement. Increasing the PCM content from N54 to N72 does not significantly further reduce density, indicating that the initial introduction of NPs has a greater impact on matrix density than the absolute amount of sodium nitrate.

In terms of structure, the porosity of the CPCM is also assessed. The grain density of FA is found to be 2.71 ± 0.05 g/cm^3. Bulk density of the CPCMs is then obtained through mass-volume measurements. The porosity is then derived from the density ratio:

$$\varphi = \left(1 - \frac{\rho_{CPCM}}{\rho_{FA}\varphi_{FA} + \rho_{Na}\varphi_{Na} + \rho_{NP}\varphi_{NP}}\right) \times 100 \quad (3)$$

where φ is the porosity of the CPCM and ρ the bulk density.

Similar to the trends in density, porosity increases with higher NP content. This suggests that NPs may introduce structural irregularities or defects, possibly by obstructing sodium nitrate infiltration within the matrix. Alternatively, the increased porosity could result from NPs hindering the flow of sodium nitrate, leading to larger voids during the sintering process. Additionally, the FA matrix might expand during cycling, contributing to defect formation and increased porosity. However, despite these trends, porosity remains generally within the statistical error range and is consistent across samples, indicating that these changes do not significantly alter the material's theoretical porosity.

3.1.3. X-ray tomography

Fig. 6 shows the pore size distribution in various CPCMs analyzed through XRT, highlighting how SiO_2 NPs affect median pore sizes across different formulations. The addition of NPs shifts the distribution

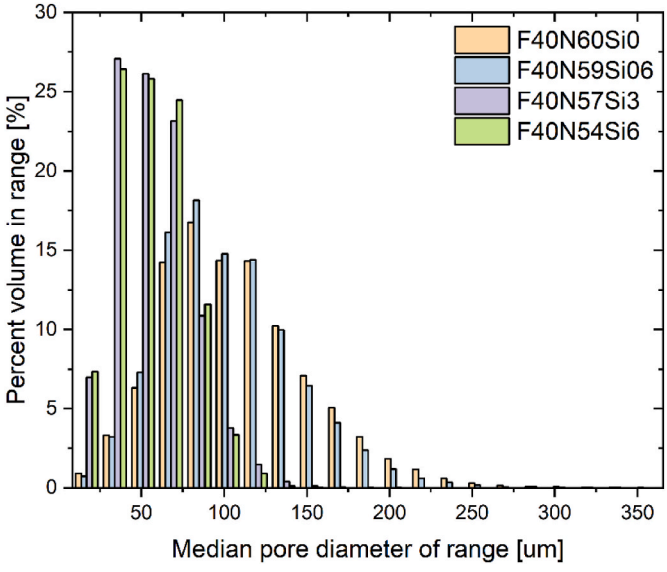


Fig. 6. Pore size distribution in various CPCMs with different SiO_2 nanoparticle contents as analyzed through XRT. The graph illustrates the influence of SiO_2 nanoparticles on the median pore sizes across different formulations.

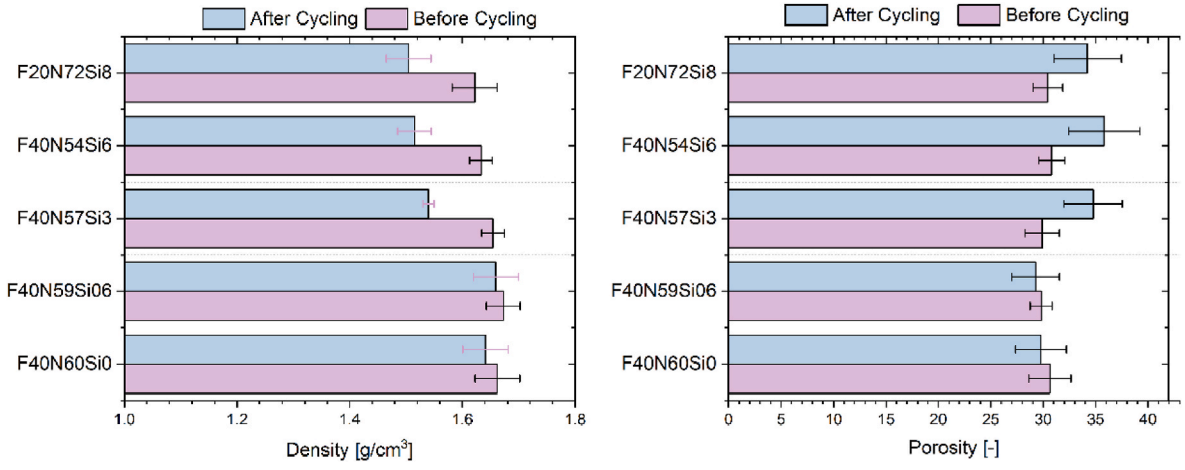


Fig. 5. Comparative illustration of density (left) and porosity (right) for various CPCMs before and after 100 thermal cycles.

towards smaller pore sizes compared to those without NPs (F40N60Si0), suggesting that they contribute to a more uniform pore structure by potentially obstructing pore formation during material preparation and sintering. The smaller, more consistent pore sizes in NP-enhanced composites indicate effective pore space management, which is crucial for maintaining material integrity under thermal stress. Notably, while overall porosity may increase with higher NP content, this does not necessarily lead to larger pores; instead, it results in a greater number of smaller, uniformly distributed pores.

This pronounced reduction in pore sizes may be attributed to several interrelated effects of SiO_2 NPs within the sodium nitrate matrix. The NPs can influence the surface tension and viscosity of molten materials. In the case of sodium nitrate, the addition of SiO_2 NPs increases its viscosity and its surface tension in an exponential and linear manner respectively [45]. This results in a denser and more restrained melt flow during the thermal processing phase, preventing the sodium nitrate from freely flowing and filling larger voids within the matrix [46]. Such behavior can thus preserve thinner pore walls and prevent their collapse during the melting and solidification cycles. This contributes to a more uniform and fine pore structure.

Another possible mechanism could be that the NPs act as nucleation sites that disrupt the normal crystal growth and melting processes. They might cause the $NaNO_3$ to crystallize around them, leading to a more distributed and fine-grained microstructure. This nucleation effect, combined with altered flow characteristics, enhances the overall uniformity and structural integrity of the composite.

These observations clearly indicate that while the mechanisms by which NPs influence pore structure are complex, their overall impact is substantial. Even at low concentrations, these effects play a critical role in the microstructure's evolution under repeated thermal cycling, highlighting the need for further detailed studies to understand the specific interactions involved.

The XRT cross-section images presented in Fig. 7 provide further visual confirmation of these observations. The composite without NPs (F40N60Si0) displays a more heterogeneous structure with larger and more irregularly distributed pores, aligning with the higher median pore size and broader distribution range observed earlier (Fig. 6). This is contrasted by the F40N59Si06 sample, where the introduction of 0.6 wt

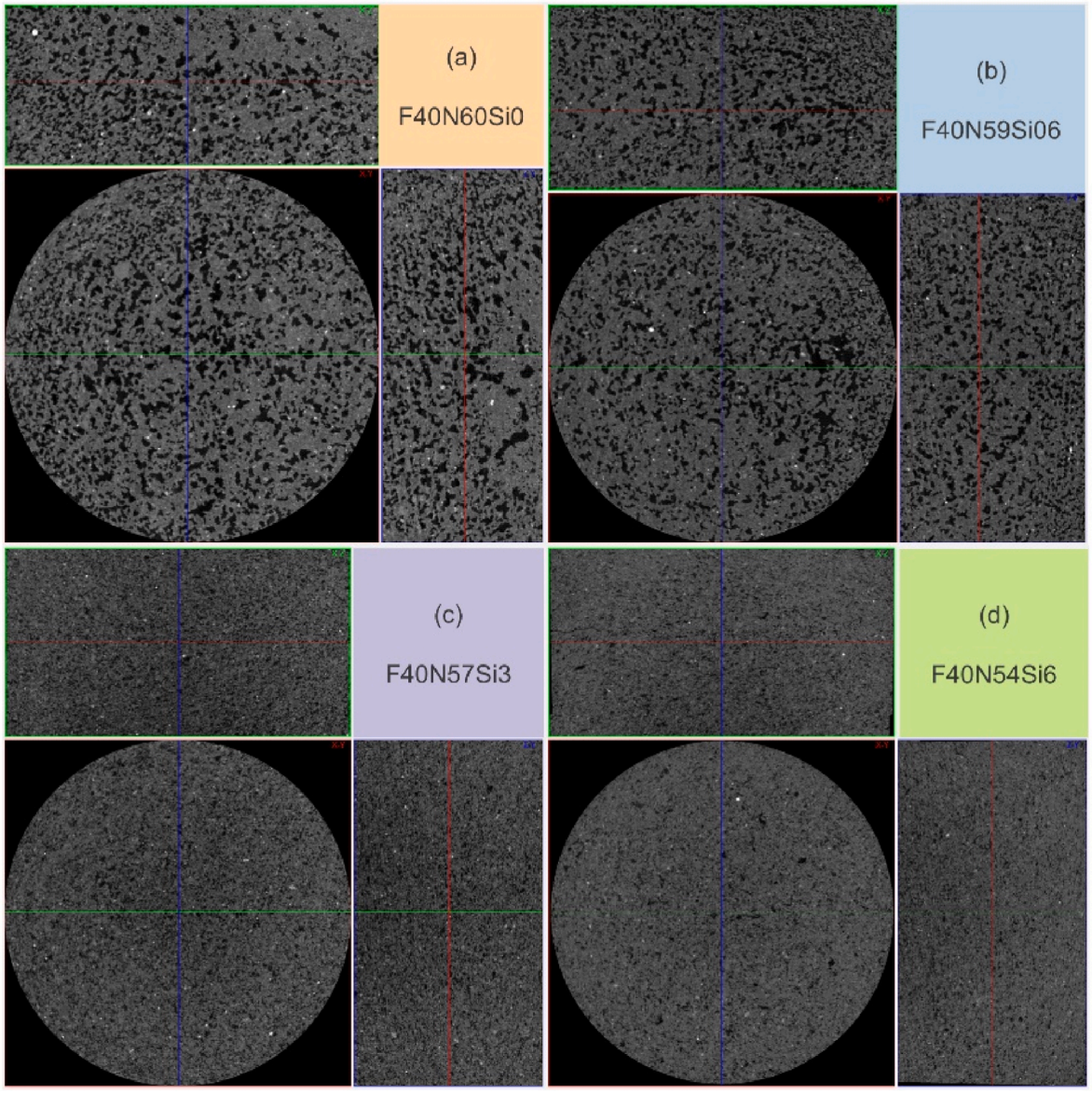


Fig. 7. X-ray tomography cross-section images of various CPCM formulations showing three orthogonal views (x-z, x-y, and z-y planes). (a) F40N60Si0, (b) F40N59Si06, (c) F40N57Si3, (d) F20N72Si8. Each pellet is 13 mm in diameter and 6 mm in height.

% SiO_2 nanoparticles significantly refines the pore structure, resulting in a denser and more uniform matrix with smaller pores.

At 3 wt% SiO_2 (F40N57Si3), the structure becomes even more refined, with uniformly small and evenly distributed pores. This suggests that the nanoparticles effectively promote a fine-grained structure and prevent the formation of larger pores.

For the composite with 8 wt% SiO_2 and higher sodium nitrate content (F20N72Si8), the images show a well-distributed pore structure similar to the F40N57Si3 sample. Despite the higher PCM content, the presence of a substantial amount of nanoparticles ensures that the pores remain small and uniformly distributed. This indicates that the NP effect on surface tension and viscosity is robust enough to maintain structural integrity even at elevated sodium nitrate levels.

3.1.4. Scanning Electron Microscopy (SEM)

The color-coded SEM images provided in Fig. 8 offer a detailed examination of the microstructural features of the CPCM formulations at varying magnifications (x50, x100, x500).

At the lowest magnification (x50), the images clearly show the overall pore distribution and size within the samples. The sample without NPs, F40N60Si0, displays larger, more irregularly shaped pores, consistent with the broader pore size distribution seen in the XRT data. As NPs are introduced (F40N59Si06), there is a noticeable reduction in pore size and a more uniform distribution. This trend continues with higher NP content in F40N57Si3 and F20N72Si8, where the pores become increasingly smaller and more evenly distributed. This visual evidence supports the hypothesis that nanoparticle addition leads to a more controlled and compact microstructure.

The medium magnification images (x100) provide a closer look at the pore walls and the distribution of sodium nitrate within the FA matrix. In F40N60Si0, the pore walls appear rough and uneven, with significant gaps indicating poor structural integrity. In contrast, the samples with NPs (F40N59Si06, F40N57Si3, and F20N72Si8) show smoother pore walls and fewer gaps, suggesting better packing and interaction between the sodium nitrate and the fly ash matrix. The nanoparticle-enhanced samples exhibit a more continuous and coherent structure.

At the highest magnification (x500), the fine details of the microstructure become apparent. The F40N60Si0 sample shows distinct and larger crystalline regions of sodium nitrate, indicative of less controlled crystallization processes. In contrast, the nanoparticle-containing samples display much finer and more homogeneous crystalline structures. This finer microstructure is likely a result of nanoparticles acting as nucleation sites. Additionally, the nanoparticle-enhanced samples show fewer microcracks and defects, further supporting the idea that nanoparticles improve the overall structural integrity.

Regarding potential structural changes like NP agglomeration or phase separation, no clear evidence was observed in the high-magnification SEM images (bottom row of Fig. 8). Significant agglomeration would typically appear as clustered NPs disrupting matrix continuity, but the samples maintained a uniform distribution, suggesting good integration within the material. No distinct boundaries indicating phase separation were observed, and the continuous structure in samples (b) and (c) further supports this. If phase separation had occurred, segregated regions or cracks from expansion/contraction mismatch would be visible. The occurrence of such instances does not appear significantly greater than in the base CPCM (without NPs), indicating no additional degradation caused by the NP addition.

3.2. Thermophysical properties of the CPCMs

3.2.1. Phase change properties

The left graph in Fig. 9 displays the latent heat values for the different CPCMs. As expected, the base $NaNO_3$ sample (0 % SiO_2) exhibits the highest latent heat, close to the theoretical maximum for pure sodium nitrate. However, it is observed that the latent heat of pure $NaNO_3$ is underestimated. This discrepancy could be due to the heating rate being too high, which was necessary for simultaneous C_p

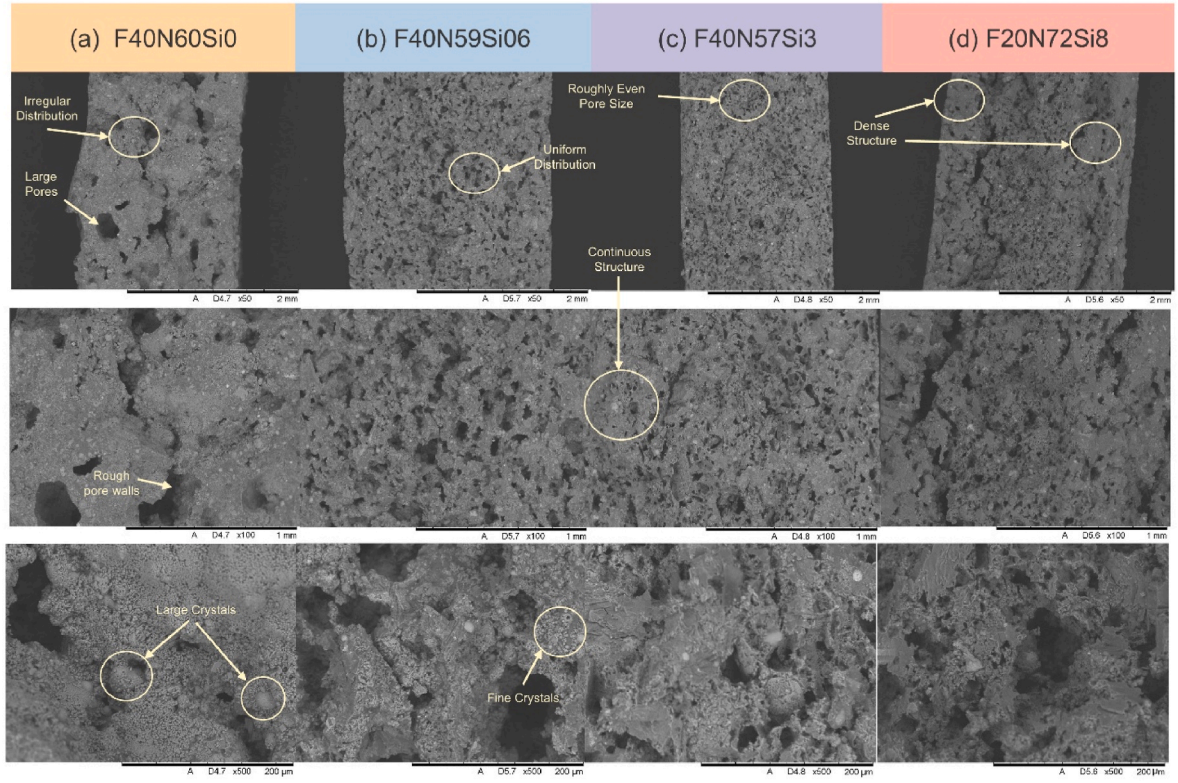


Fig. 8. SEM cross-sectional images of CPCM samples at different magnifications (x50, x100, x500). (a) F40N60Si0, (b) F40N59Si06, (c) F40N57Si3, (d) F20N72Si8. The scale bar is 2 mm, 1 mm and 200 μm from top to bottom row respectively.

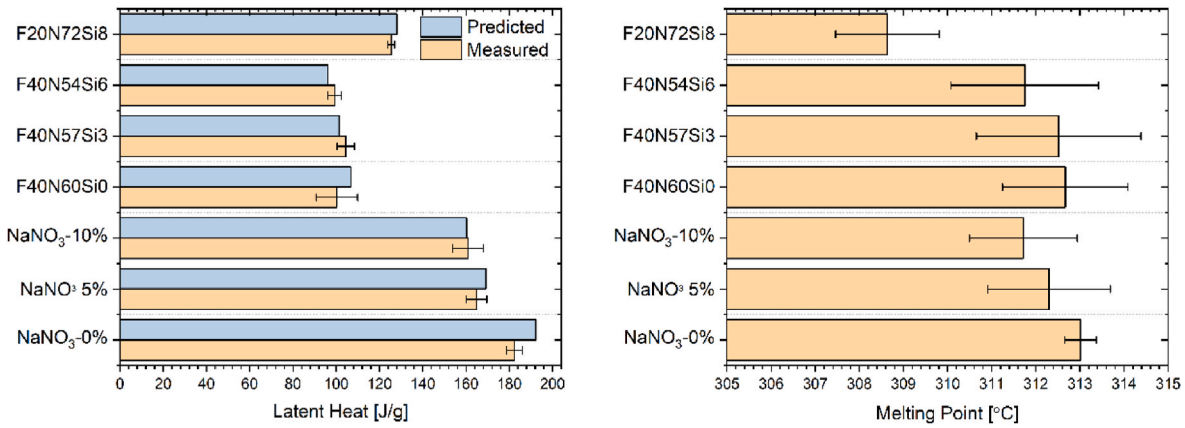


Fig. 9. Comparison of latent heat between measured and predicted values for various CPCM formulations (left) and melting point (right), including different SiO_2 nanoparticle contents and sodium nitrate percentages.

measurements. Higher heating rates can lead to inaccuracies because the sample does not have sufficient time to reach thermal equilibrium, potentially causing incomplete phase transitions and heat flow measurement issues. The addition of SiO_2 NPs slightly reduces the latent heat capacity, which is a common observation when introducing secondary materials into a pure phase change material due to the dilution effect and possible reduction in PCM volume fraction [47]. Nevertheless, the measured latent heat values are within the error range of the predicted values. The fact that the latent heat values for CPCMs, even after thermal cycling, are close to the predicted values is a testament to the sample's stability, indicating no leakage and maintaining a consistent PCM content.

The right graph in Fig. 9 displays the melting points of various CPCMs, showing that the melting point of $NaNO_3$ remains relatively stable across different NP concentrations, with only minor variations. The base $NaNO_3$ sample has a melting point of approximately 313 °C, which is slightly overpredicted. This discrepancy, likely due to factors such as a high heating rate, is consistent across the samples.

The introduction of SiO_2 nanoparticles generally leads to a slight reduction in the melting point. This trend, within the error bars, aligns with the known effect of adding impurities to a PCM, which can disrupt the crystal lattice and lower the melting point [47]. Further reduction with increased NP content might be due to the NPs affecting the crystallization process.

Moreover, the thermal conductivity of the composites can also play a role in the observed melting points. The addition of SiO_2 nanoparticles is known to enhance the thermal conductivity of the PCM, which could lead to a more uniform temperature distribution during heating. This uniformity can result in a slightly lower melting point, as the heat is more effectively distributed throughout the material. Additionally, PCM encapsulation within the FA matrix can influence the melting behavior.

3.2.2. Specific heat capacity

The specific heat capacity (C_p) values of FA are close to what is expected from literature sources (Fig. 10) [48,49]. These were the first C_p measurements for Greek sourced FA, and therefore cannot be compared directly. They exhibit a slightly higher C_p, which can be attributed to its larger CaO content compared to most reported sources. This likely influences the C_p by reacting with water to form calcium hydroxide ($Ca(OH)_2$) and other hydration products. These reactions increase the amount of chemically bound water, which has a higher C_p, thereby raising the overall C_p.

For $NaNO_3$, the C_p in the solid phase was not compared to literature values due to not many available repots, because of the complexity of accurately determining this parameter. This complexity arises from a solid-solid phase transition in $NaNO_3$ with an onset around 270 °C, making precise determination challenging [50]. When examining the CPCMs, it is observed that increasing the silica content results in a slight increase in C_p, although this change is within the measurement error.

The predicted C_p values are derived from classical mixing theory. For silica, a value of 1.12 J/gK is used based on Engelman et al. [51]. For the $NaNO_3$-SiO_2 mixtures, the C_p of $NaNO_3$ as measured in this study is utilized. Similarly, for predicting the C_p of CPCMs, the measured values for FA and $NaNO_3$ are employed. The results indicate that the measured

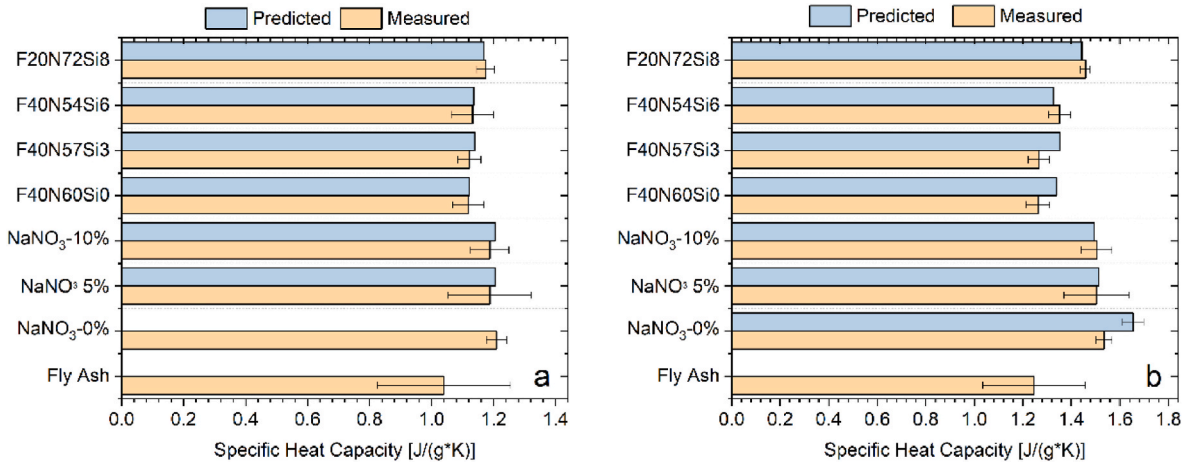


Fig. 10. Comparison of predicted and measured C_p values for various PCM and CPCM formulations for solid phase (a) and liquid phase (b).

values are generally within the range of the predicted values, confirming the reliability of mixing theory in the solid phase.

In the liquid phase, the specific heat capacity of FA is higher than in the solid phase, which is expected as C_p tends to increase with temperature. The C_p of $NaNO_3$ is lower than literature reported [52]. The lower C_p could be attributed to experimental variations or measurement conditions.

For the $NaNO_3$-5 % and $NaNO_3$-10 % samples, the C_p is somewhat lower than pure $NaNO_3$, since the addition of SiO_2, which has a lower C_p than molten $NaNO_3$, reduces the overall C_p. The measured values align well with the predictions, which is consistent with the theory that adding large amounts of nanoparticles to molten salt above 1–2 wt% does not significantly enhance its C_p since these tend to agglomerate after repeated thermal cycling [47].

In the case of CPCMs, a slight underprediction is observed. This discrepancy might be due to the complex interactions within the CPCM that are not fully captured by the predictive model. Increasing the nanoparticle content generally results in a higher C_p, although the values remain within the error range, showing no clear trend. However, increasing the PCM content in the CPCM results in the highest C_p values. At very high nanoparticle contents within the CPCM, a slight overprediction is observed. This could be within the error margin or possibly due to the nanoparticles being partially mixed in the salt, leading to a minor increase in C_p.

Looking at F40N54Si6, this sample contains the highest wt.% of NPs in the salt. Given that some agglomeration and redistribution of NPs is expected, it is reasonable to hypothesize that having the highest total NP content also results in the highest fraction of well-dispersed NPs. This could explain the observed higher C_p values and, consequently, the slightly higher ESD in this sample.

3.2.3. Thermal conductivity

The thermal conductivity of all samples decreases with increasing temperature up to around 300 °C, after which it starts to increase again (Fig. 11, left). As the temperature approaches 300 °C, the thermal conductivity drops because this is the region where $NaNO_3$ undergoes a solid-solid phase transition (at approximately 275 °C) and then melts (around 306 °C). During these phase transitions, the material absorbs a significant amount of energy without a corresponding rise in temperature, leading to an increased C_p and a disruption in the thermal pathways, which reduces the overall thermal conductivity.

The reduction in thermal conductivity in this region is reflected in the C_p for which the calculations are based on a linear interpolation from values around 250 °C–350 °C. This approach does not account for the actual spike in C_p due to latent heat during phase transitions.

Beyond 300 °C, the thermal conductivity shows an increase, within the margin of error. This unexpected trend has been previously reported in molten nitrate salts [53]. The exact reason is unclear but could be influenced by several factors such as measurement technique differences, sample purity, and sample volume effects. In the case of the CPCMs reported in this work the trend, within error margin, is likely due to uncertainties in C_p measurements, which affect LFA-derived thermal conductivity. Ideally, the latter should be validated using an alternative method, but this was beyond the scope and capabilities of the present study.

Comparing different materials, $NaNO_3$ demonstrates consistently lower thermal conductivity than any CPCM across the whole temperature range. F40N60Si0 consistently shows the highest thermal conductivity. This is expected because its porosity is the lowest (Fig. 5).

Among the NP-enhanced samples, F40N54Si6 demonstrates the highest thermal conductivity. This can be attributed to its higher content of SiO_2 (6 %), which has a significantly higher thermal conductivity than that of $NaNO_3$ [54]. Additionally, the porosity of F40N54Si6 is similar to that of F40N57Si3 (within the error margin). A higher SiO_2 content in F40N54Si6 results in a slightly higher thermal conductivity compared to F40N57Si3.

F20N72Si8 has the lowest thermal conductivity among the CPCMs. This is expected due to its very low content of FA and very high content of $NaNO_3$. However, it is crucial to note that overall, increasing the PCM content from 57 % to 72 % does not significantly reduce the thermal conductivity, especially in the liquid phase. This suggests that while increasing PCM content typically reduces thermal conductivity, the SiO_2 NPs help mitigate this effect by creating a more interconnected network that enhances heat transport. This balances the reduction caused by the higher PCM fraction.

In terms of average thermal conductivities the base $NaNO_3$ sample has the lowest thermal conductivity. Among the CPCMs with added NPs, F40N54Si6 has the highest, followed by F40N57Si3 and F20N72Si8. To quantify the enhancement: F40N60Si0 shows an enhancement of approximately 115.9 %, F40N57Si3 a 61.3 % increase, F40N54Si6 exhibits an 77.5 % improvement, and F20N72Si8 displays an enhancement of 27.6 % compared to the base salt. This highlights the substantial impact of NPs coupled with encapsulation on enhancing the thermal conductivity of a PCM.

While F40N60Si0 exhibits irregularly shaped pores and significant gaps (Figs. 7 and 8), it still demonstrates the highest thermal conductivity among the samples (Fig. 11, right). This can be attributed to the fact that FA, being a solid matrix material, inherently has a higher

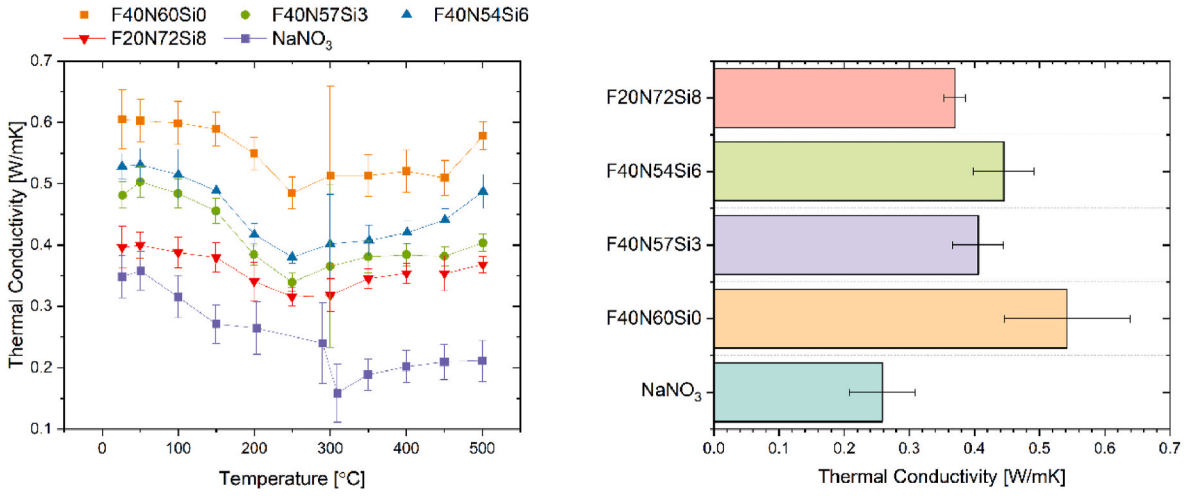


Fig. 11. (Left) Temperature-dependent thermal conductivity of CPCMs with different compositions: F40N60Si0, F40N57Si3, F40N54Si6, and F20N72Si8. (Right) Average thermal conductivity comparison of various CPCMs throughout the evaluated temperature range.

thermal conductivity compared to $NaNO_3$. Although increased porosity is detrimental to thermal conductivity, the impact is not sufficient to offset the inherently higher conductivity of FA. This explains why F40N60Si0 outperforms the other samples in thermal conductivity, despite its structural irregularities.

The addition of SiO_2 NPs influences the thermal conductivity in two primary ways. Firstly, amorphous SiO_2 has a higher intrinsic thermal conductivity of 1.8 W/mK [55] compared to $NaNO_3$ (around 0.3 W/mK [53]) and FA. Therefore, adding SiO_2 nanoparticles can enhance the overall thermal transport properties of the composite. Secondly, the presence of SiO_2 can improve the thermal connectivity within the composite by creating more efficient heat conduction pathways. The nanoparticles can bridge gaps between the matrix and the PCM, facilitating better phonon transport, which are the primary carriers of heat in non-metallic solids, leading to an increase in thermal conductivity.

3.2.4. Coefficient of thermal expansion

The base sample, F40N60Si0, which contains no NPs, has the highest CTE value at approximately 25 $°C^{-1}$ (Fig. 12). The addition of SiO_2 nanoparticles significantly reduces the CTE values. For instance, F40N59Si06, with a small amount of SiO_2, shows a substantial decrease in CTE. Increasing the SiO_2 content to 3 wt% (F40N57Si3) results in an even lower CTE, indicating enhanced thermal stability. However, further increasing the SiO_2 content to 6 wt% (F40N54Si6) does not show a significant improvement beyond the reduction observed at 3 wt% SiO_2, suggesting a threshold beyond which additional nanoparticles do not further enhance thermal stability.

Notably, the sample with a high PCM content, F20N72Si8, maintains a low CTE comparable to SiO_2 enhanced samples with lower PCM content. Despite the high $NaNO_3$ content, it exhibits a CTE similar to that of F40N54Si6. This demonstrates that the addition of SiO_2 effectively stabilizes the composite's thermal expansion even at high PCM contents, which is highly valuable for maintaining structural integrity during thermal cycling. It is also important to consider that the enhancement in CTE is substantial given that the CTE of $NaNO_3$ alone is significantly higher.

When NPs are introduced into a liquid, they interact with surrounding molecules, forming a structured interfacial layer that restricts molecular mobility [55]. This ordering effect, observed in molecular dynamics simulations and experimental studies on nanofluids, reduces volumetric expansion upon heating [55]. Additionally, the CTE value of SiO_2 is significantly lower CTE values than that of $NaNO_3$ [50]. By introducing a solid-phase additive with a much lower CTE, the overall CTE of the mixture is reduced, a trend validated in certain nanofluids based on simple mixing theory [56]. Research on nanofluids has shown that increasing the nanoparticle concentration tends to decrease the overall CTE [57]. However, at higher concentrations, percolation effects or aggregation can occur, which may limit further reductions in CTE beyond a threshold value. This can explain the possible threshold observed here at 3 wt %.

While the above has been somewhat established in cases of organic liquids, no research specifically examines this effect in molten salts, presenting a significant knowledge gap. However, although direct experimental validation for molten salts is lacking, the observed CTE reduction in these CPCMs aligns with fundamental principles, suggesting that SiO_2 NPs effectively improve CTE.

3.2.5. Energy storage density and material assessment

FA exhibits the lowest energy storage density (ESD), as expected, due to its relatively low specific heat capacity and the absence of a significant phase change enthalpy (Fig. 13). $NaNO_3$, on the other hand, shows the highest ESD among the individual componentsdue to high latent heat and C_p.

The CPCM samples demonstrate varying levels of ESD depending on the composition and the presence of SiO_2. It is clear that adding SiO_2 nanoparticles does not significantly enhance ESD, which is anticipated since nanoparticles themselves are solid materials with C_p similar to FA and no latent heat. F40N60Si0, shows an ESD comparable to those with added nanoparticles, such as F40N57Si3 and F40N54Si6. F20N72Si8 the sample with the highest PCM content exhibits the highest ESD among the CPCMs, due to its higher $NaNO_3$ content.

This indicates that the primary role of nanoparticles is not in enhancing ESD but in stabilizing the composite structure and improving other thermal properties. Through this nanoparticle addition enables higher ESD but also improves other thermal properties like CTE or thermal conductivity.

This is clearer when looking at the relationship between thermal conductivity and ESD in CPCMs is influenced by both SiO_2 nanoparticle content and PCM concentration. At 60 wt% $NaNO_3$, adding SiO_2 initially reduces both thermal conductivity and ESD, with 3 wt% SiO_2 resulting in the lowest values (0.406 W/mK, 528 J/g). However, increasing SiO_2 to 6 wt% shows a slight recovery in both properties, suggesting a balance between nanoparticle dispersion and PCM displacement. At higher PCM content (72 wt% $NaNO_3$, 8 wt% SiO_2), ESD **increases significantly** due to the larger PCM fraction, while thermal conductivity remains **comparable to that of the 60 wt% $NaNO_3$ sample with lower nanoparticle content**. This demonstrates that **higher PCM content can be achieved without drastically compromising thermal performance**,

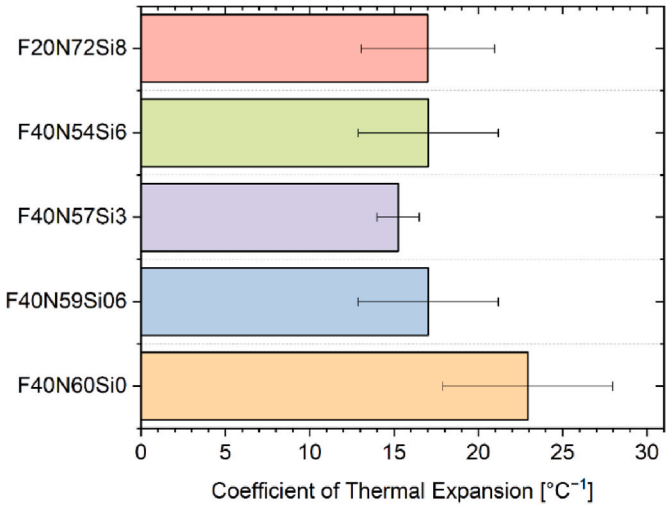


Fig. 12. Coefficient of Thermal Expansion for various CPCMs: F40N60Si0, F40N59Si06, F40N57Si3, F40N54Si6, and F20N72Si8.

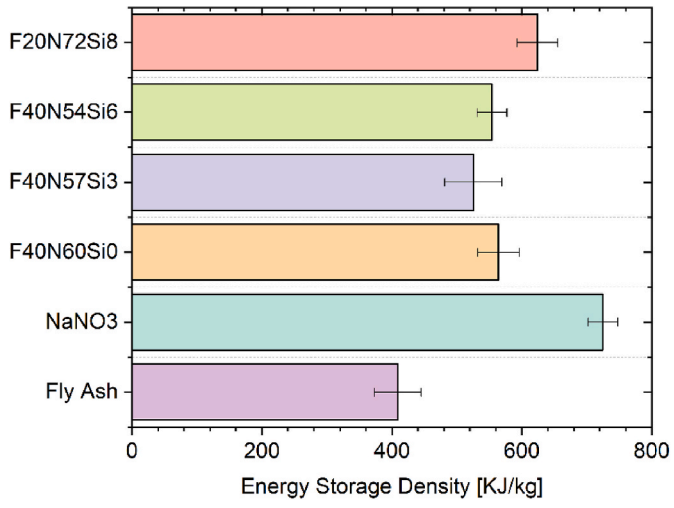


Fig. 13. Energy storage density from 25 to 400 °C of various CPCM samples and reference materials (Fly Ash and $NaNO_3$).

as long as SiO_2 concentration is optimized for structural stability. The absence of stable formulations at 80 wt% $NaNO_3$ with lower SiO_2 content prevents a direct analysis of the trade-off at this range, as additional SiO_2 was required to maintain integrity. These findings reinforce the need for nanoparticle optimization to balance enhanced energy storage with thermal conductivity, a crucial factor for TES applications.

The FA based composite PCM developed in this work exhibits an ESD of 632.38 J/g, which is within the range of existing $NaNO_3$-based composite PCMs. While its total energy storage density is comparable to other materials (Table 3), its key advantage lies in achieving a high PCM content of 72 wt%, whereas most previous studies are limited to 60 wt%. Its formulation allows for a greater latent heat contribution, which is particularly beneficial for applications operating near the phase transition of $NaNO_3$.

In terms of thermal conductivity (0.369 W/m·K), the composite performs better than others such as $NaNO_3$/M-DC4 (0.220 W/m·K) and in par with other reported in the literature such as $NaNO_3$/diatomite (0.453 W/m·K) but remains lower than $NaNO_3$/semi-coke ash, graphite (1.844 W/m·K) and $NaNO_3$/waste foundry sand (1.03 W/m·K). The higher conductivity in these materials is likely due to the presence of graphite in the fly ash matrix and decomposed polymers (carbon) in the foundry sand, which improve thermal conductivitys. Future work could explore the incorporation of small amounts of graphite or other conductive additives to enhance thermal transport while maintaining the benefits of high $NaNO_3$ content.

Table 3
Comparison of energy storage density and thermal conductivity of various $NaNO_3$-based CPCMs.

Material	Energy Storage Density (J/g) (25–400 °C)	Thermal Conductivity (W/m·K)
$NaNO_3$/fly ash (this work)	632.38	0.389
$NaNO_3$/semi-coke ash, graphite [58]	513.75	1.844
$NaNO_3$/Sludge-incinerated ash [59]	497.66	0.493
$NaNO_3$/M-DC4 [60]	627.15	0.220
$NaNO_3$/diatomite [61]	654.39	0.453
$NaNO_3$/waste foundry sand [62]	628.00	1.03

4. Conclusions

Heavy industries play a crucial role in the economy but face challenges in achieving carbon-neutral operations. Industrial heating processes, consuming 70 % of the sector's energy, generate substantial waste heat, offering significant recovery opportunities. TES solutions, particularly LHTES, provide efficient WHR with higher energy density and minimal temperature variation. However, LHTES faces challenges like limited thermal conductivity and large volume changes during phase transitions. Encapsulating PCMs in porous matrices to fabricate CPCMs can address these issues, although traditional CPCMs have low PCM content. This study introduces NPs enabling CPCMs with a PCM content over 72 % and drastically improved thermal performance. The main outcomes are.

- SiO_2 NPs improved the structural stability of CPCMs, allowing higher PCM content without compromising integrity, by enhancing the cohesion and mechanical stability of the composites.
- F20N72Si8 maintained structural integrity with 72 % $NaNO_3$, surpassing the 60 % PCM limit achieved without any NPs, demonstrating the effectiveness of nanoparticle addition in increasing PCM capacity.
- Encapsulation nearly doubled the thermal conductivity of pure $NaNO_3$, providing enhanced heat transfer capabilities crucial for efficient TES.
- Addition of NPs did not further enhance the thermal conductivity but was able to maintain it even at high PCM content.
- Adding SiO_2 NPs substantially reduced the CTE, compared to base CPCMs up to an extent. What is notable is that even at high PCM contents the CTE values still remained low, mitigating the risks of thermal expansion-related issues.
- F20N72Si8 showed only a ~14 % decrease in ESD compared to pure $NaNO_3$ but substantially improved thermal conductivity by 28 %.

These findings highlight the significant advancements achieved with NP-enhanced CPCMs. Achieving high PCM content in a stable composite is a notable innovation. This approach transforms materials like FA, which previously could not maintain structural integrity with PCM content above 60 %, into viable candidates for TES applications. When using materials with better thermal properties and grain structure, the benefits of this encapsulation strategy could be even more pronounced, paving the way for more efficient and robust TES systems. Future research should optimize the balance between PCM content and NP concentration to maximize energy storage density and enhance thermal properties. Additionally, exploring matrix materials with better thermal properties and grain structures could further improve CPCM performance in TES systems.

CRediT authorship contribution statement

A. Anagnostopoulos: Writing – review & editing, Writing – original draft, Visualization, Validation, Methodology, Investigation, Funding acquisition, Formal analysis, Data curation, Conceptualization. **M. Elena Navarro:** Writing – review & editing, Writing – original draft, Visualization, Validation, Methodology, Investigation, Formal analysis, Conceptualization. **Zhu Jiang:** Writing – review & editing, Methodology, Investigation, Data curation. **Yulong Ding:** Resources, Project administration, Funding acquisition.

Declaration of competing interest

The authors declare that they have no known competing financial interests or personal relationships that could have appeared to influence the work reported in this paper.

Acknowledgements

The authors would like to acknowledge the Narodowe Centrum Nauki funding agency for supporting this research through the project:2022/47/D/ST8/03239.

Data availability

Data will be made available on request.

References

[1] O. Ellabban, H. Abu-Rub, F. Blaabjerg, Renewable energy resources: current status, future prospects and their enabling technology, Renew. Sustain. Energy Rev. 39 (2014), https://doi.org/10.1016/j.rser.2014.07.113.
[2] European Commission. Renewable Energy Targets, European Commission (2023).
[3] IEA. Global Energy Review 2021, IEA, Paris, 2021. https://www.iea.org/reports/global-energy-review-2021.
[4] R. Agathokleous, G. Bianchi, G. Panayiotou, L. Aresti, M.C. Argyrou, G.S. Georgiou, S.A. Tassou, H. Jouhara, S.A. Kalogirou, G.A. Florides, P. Christodoulides, Waste Heat Recovery in the EU industry and proposed new technologies, Energy Proc. 161 (2019) 489–496, https://doi.org/10.1016/j.egypro.2019.02.064.
[5] L. Miró, J. Gasia, L.F. Cabeza, Thermal energy storage (TES) for industrial waste heat (IWH) recovery: a review, Appl. Energy 179 (2016), https://doi.org/10.1016/j.apenergy.2016.06.147.
[6] A.I. Fernández, C. Barreneche, L. Miró, S. Brückner, L.F. Cabeza, A.I. Fernández, C. Barreneche, L. Miró, L.F. Cabeza, S. Brückner, Waste heat recovery using thermal energy storage, in: Adv. Therm. Energy Storage Syst., 2021, https://doi.org/10.1016/b978-0-12-819885-8.00022-x.

[7] A. Palacios, C. Barreneche, M.E. Navarro, Y. Ding, Thermal energy storage technologies for concentrated solar power – a review from a materials perspective, Renew. Energy (2019), https://doi.org/10.1016/j.renene.2019.10.127.

[8] H. Jouhara, A. Żabnieńska-Góra, N. Khordehgah, D. Ahmad, T. Lipinski, Latent thermal energy storage technologies and applications: a review, Int. J. Thermofluids 5–6 (2020), https://doi.org/10.1016/j.ijft.2020.100039.

[9] F. Jiang, L. Zhang, X. She, C. Li, D. Cang, X. Liu, Y. Xuan, Y. Ding, Skeleton materials for shape-stabilization of high temperature salts based phase change materials: a critical review, Renew. Sustain. Energy Rev. 119 (2020) 109539, https://doi.org/10.1016/j.rser.2019.109539.

[10] J. Li, R. Li, T. Li, Y. Ma, Advancements in the utilization of nanocarbon sphere composites in supercapacitor, Adv. Compos. Hybrid Mater. 2025 81 (8) (2025) 1–34, https://doi.org/10.1007/S42114-024-01187-9.

[11] Y. Liu, K. Gao, H. Yi, L. Xia, S. Song, Flexible MoS2/CNF/PEG phase change film with superior photothermal conversion and thermal energy storage, Sol. Energy Mater. Sol. Cells 282 (2025) 113376, https://doi.org/10.1016/J.SOLMAT.2024.113376.

[12] Z. Mai, K. You, J. Chen, X. Sheng, Y. Chen, Perspective on phase change composites in high-efficiency solar-thermal energy storage, Appl. Phys. Lett. 126 (2025), https://doi.org/10.1063/5.0248794/3333352.

[13] X. He, W. Zhang, Y. Yang, G. Yang, Y. Zhang, G. Huang, J. Luo, C. Cui, X. Sheng, Triple-network structured phase change composite based on “rod-brush” CNTs-CFs with high thermal conductivity, Compos. Sci. Technol. 262 (2025) 111080, https://doi.org/10.1016/J.COMPSCITECH.2025.111080.

[14] B. Liu, Y. Yang, D. Huang, R. Liang, X. Jiang, L. Zhang, Y. Chen, G. Sun, X. Sheng, An innovative MXene modified melamine foam shape-stabilized hydrated salt-based composite PCM for indoor thermal comfort and energy saving in buildings, Constr. Build. Mater. 466 (2025) 140289, https://doi.org/10.1016/J.CONBUILDMAT.2025.140289.

[15] M.Y. Abdelsalam, H.M. Teamah, M.F. Lightstone, J.S. Cotton, Hybrid thermal energy storage with phase change materials for solar domestic hot water applications: direct versus indirect heat exchange systems, Renew. Energy 147 (2020), https://doi.org/10.1016/j.renene.2019.08.121.

[16] Z. Jiang, A. Palacios, B. Zou, Y. Zhao, W. Deng, X. Zhang, Y. Ding, A review on the fabrication methods for structurally stabilised composite phase change materials and their impacts on the properties of materials, Renew. Sustain. Energy Rev. 159 (2022), https://doi.org/10.1016/j.rser.2022.112134.

[17] M.E. Navarro, A.P. Trujillo, Z. Jiang, Y. Jin, Y. Zhang, Y. Ding, Chapter 7: manufacture of thermal, Energy Storage Mater. (2021) 121–190, https://doi.org/10.1039/9781788019842-00121.

[18] Z. Ge, F. Ye, H. Cao, G. Leng, Y. Qin, Y. Ding, Carbonate-salt-based composite materials for medium- and high-temperature thermal energy storage, Particuology 15 (2014) 77–81, https://doi.org/10.1016/j.partic.2013.09.002.

[19] L. Sang, F. Li, Y. Xu, Form-stable ternary carbonates/MgO composite material for high temperature thermal energy storage, Sol. Energy 180 (2019) 1–7, https://doi.org/10.1016/j.solener.2019.01.002.

[20] G. Xu, G. Leng, C. Yang, Y. Qin, Y. Wu, H. Chen, L. Cong, Y. Ding, Sodium nitrate – diatomite composite materials for thermal energy storage, Sol. Energy 146 (2017) 494–502, https://doi.org/10.1016/j.solener.2017.03.003.

[21] A. Miliozzi, M. Chieruzzi, L. Torre, Experimental investigation of a cementitious heat storage medium incorporating a solar salt/diatomite composite phase change material, Appl. Energy (2019), https://doi.org/10.1016/j.apenergy.2019.05.090.

[22] C. Li, Q. Li, L. Cong, F. jiang, Y. Zhao, C. Liu, Y. Xiong, C. Chang, Y. Ding, MgO based composite phase change materials for thermal energy storage: the effects of MgO particle density and size on microstructural characteristics as well as thermophysical and mechanical properties, Appl. Energy (2019), https://doi.org/10.1016/j.apenergy.2019.04.094.

[23] A. Anagnostopoulos, M.E. Navarro, M. Stefanidou, Y. Ding, G. Gaidajis, Red mud-molten salt composites for medium-high temperature thermal energy storage and waste heat recovery applications, J. Hazard Mater. 413 (2021), https://doi.org/10.1016/j.jhazmat.2021.125407.

[24] A. Anagnostopoulos, M.E. Navarro, M. Stefanidou, P. Seferlis, G. Gaidajis, Y. Ding, Effect of carbon on the performance of red mud-molten salt composites for thermal management and waste heat recovery applications, J. Energy Storage 44 (2021) 103363, https://doi.org/10.1016/j.est.2021.103363.

[25] A. Qu, J. Zhao, H. Peng, F. Jiang, Recycled blast furnace slag to form-stabilize NaNO3 with high performance for high-temperature thermal energy storage, J. Energy Storage 55 (2022) 105870, https://doi.org/10.1016/J.EST.2022.105870.

[26] M. Ji, L. Lv, A. Zhang, H. Zhou, Research on dolomite-based shape-stabilized phase change materials for thermal energy storage: feasibility study of raw and calcined dolomite as skeleton support materials, J. Energy Storage 75 (2024) 109745, https://doi.org/10.1016/J.EST.2023.109745.

[27] F. Jiang, L. Zhang, Z. Jiang, C. Li, D. Cang, X. Liu, Y. Xuan, Y. Ding, Diatomite-based porous ceramics with high apparent porosity: pore structure modification using calcium carbonate, Ceram. Int. 45 (2019) 6085–6092, https://doi.org/10.1016/J.CERAMINT.2018.12.082.

[28] Y. Deng, J. Li, T. Qian, W. Guan, X. Wang, Preparation and characterization of KNO3/diatomite shape-stabilized composite phase change material for high temperature thermal energy storage, J. Mater. Sci. Technol. (2017), https://doi.org/10.1016/j.jmst.2016.02.011.

[29] Q. Yu, Y. Lu, C. Zhang, X. Zhang, Y. Wu, A. Sciacovelli, Preparation and thermal properties of novel eutectic salt/nano-SiO2/expanded graphite composite for thermal energy storage, Sol. Energy Mater. Sol. Cells 215 (2020) 110590, https://doi.org/10.1016/j.solmat.2020.110590.

[30] Y.R. Guo, Y. Liu, G.Q. Zhang, Z.F. Deng, G.Z. Xu, B.R. Li, Effect of SiO 2 on the thermal stability of carbonate/MgO composite for thermal energy storage, IOP Conf. Ser. Mater. Sci. Eng. 504 (2019) 012011, https://doi.org/10.1088/1757-899X/504/1/012011.

[31] F. Ye, Z. Ge, Y. Ding, J. Yang, Multi-walled carbon nanotubes added to Na2CO3/MgO composites for thermal energy storage, Particuology 15 (2014) 56–60, https://doi.org/10.1016/j.partic.2013.05.001.

[32] F. Jiang, X. Ling, L. Zhang, D. Cang, Y. Ding, Improved thermal conductivity of form-stable NaNO3: using the skeleton of porous ceramic modified by SiC, Sol. Energy Mater. Sol. Cells 231 (2021) 111310, https://doi.org/10.1016/J.SOLMAT.2021.111310.

[33] Q. Luo, X. Liu, H. Wang, Q. Xu, Y. Tian, T. Liang, Q. Liu, Z. Liu, X. Yang, Y. Xuan, Y. Li, Y. Ding, Synergetic enhancement of heat storage density and heat transport ability of phase change materials inlaid in 3D hierarchical ceramics, Appl. Energy 306 (2022) 117995, https://doi.org/10.1016/j.apenergy.2021.117995.

[34] W. Song, Y. Lu, Z. Fan, Y. Wu, Preparation and thermophysical properties of sodium nitrate/nanoparticle/expanded graphite composite heat storage material, Front. Energy Res. 10 (2022) 878747, https://doi.org/10.3389/FENRG.2022.878747/BIBTEX.

[35] Q. Yu, C. Zhang, Y. Lu, Q. Kong, H. Wei, Y. Yang, Q. Gao, Y. Wu, A. Sciacovelli, Comprehensive performance of composite phase change materials based on eutectic chloride with SiO2 nanoparticles and expanded graphite for thermal energy storage system, Renew. Energy 172 (2021) 1120–1132, https://doi.org/10.1016/J.RENENE.2021.03.061.

[36] Z. Kang, S. Huang, X. Liu, Y. Zhang, M. He, A novel high temperature eutectic salt and its composite with enhanced high conductivity, J. Energy Storage 59 (2023), https://doi.org/10.1016/j.est.2022.106409.

[37] K. Bashirnezhad, S. Bazri, M.R. Safaei, M. Goodarzi, M. Dahari, O. Mahian, A. S. Dalkiliça, S. Wongwises, Viscosity of nanofluids: a review of recent experimental studies, Int. Commun. Heat Mass Transf. 73 (2016) 114–123, https://doi.org/10.1016/J.ICHEATMASSTRANSFER.2016.02.005.

[38] A.K. Nayak, R.K. Singh, P.P. Kulkarni, Measurement of volumetric thermal expansion coefficient of various nanofluids, Tech. Phys. Lett. 36 (2010) 696–698, https://doi.org/10.1134/S1063785010080055, 2010 368.

[39] P. Estellé, D. Cabaleiro, G. Żyła, L. Lugo, S.M.S. Murshed, Current trends in surface tension and wetting behavior of nanofluids, Renew. Sustain. Energy Rev. 94 (2018) 931–944, https://doi.org/10.1016/j.rser.2018.07.006.

[40] N.A. Che Sidik, M. Mahmud Jamil, W.M.A. Aziz Japar, I. Muhammad Adamu, A review on preparation methods, stability and applications of hybrid nanofluids, Renew. Sustain. Energy Rev. 80 (2017) 1112–1122, https://doi.org/10.1016/j.rser.2017.05.221.

[41] G. Kostakis, Characterization of the fly ashes from the lignite burning power plants of northern Greece based on their quantitative mineralogical composition, J. Hazard Mater. 166 (2009), https://doi.org/10.1016/j.jhazmat.2008.12.007.

[42] J.M. Fox, Changes in Fly Ash with Thermal Treatment, 2005 WorldofCoal Ash (WOCA), April 11-15, Lexington, Kentucky,USA, 2005.

[43] Y. Zhang, Q. Sun, J. Geng, Microstructural characterization of limestone exposed to heat with XRD, SEM and TG-DSC, Mater. Charact. 134 (2017), https://doi.org/10.1016/j.matchar.2017.11.007.

[44] T.V. Kumar, A.S. Chary, A.M. Awasthi, S. Bhardwaj, S.N. Reddy, Effect of nano SiO2 on properties of structural, thermal and ionic conductivity of 85.32[NaNO3]–14.68[Sr(NO3)2] mixed system, Ionics 21 (2015), https://doi.org/10.1007/s11581-014-1301-2.

[45] A. Anagnostopoulos, A. Palacios, M.H. Navarro, S. Fereres, Y. Ding, Effect of SiO2 nanoparticle addition on the wetting and rheological properties of solar salt, Sol. Energy Mater. Sol. Cells 210 (2020) 110483, https://doi.org/10.1016/j.solmat.2020.110483.

[46] A. Anagnostopoulos, M.E. Navarro, Y. Ding, Microstructural improvement of solar salt based MgO composites through surface tension/wettability modification with SiO2 nanoparticles, Sol. Energy Mater. Sol. Cells 238 (2022) 111577, https://doi.org/10.1016/J.SOLMAT.2022.111577.

[47] B. Muñoz-Sánchez, J. Nieto-Maestre, I. Iparraguirre-Torres, A. García-Romero, J. M. Sala-Lizarraga, Molten salt-based nanofluids as efficient heat transfer and storage materials at high temperatures. An overview of the literature, Renew. Sustain. Energy Rev. 82 (2018) 3924–3945, https://doi.org/10.1016/j.rser.2017.10.080.

[48] P. Shetty, V. Atgur, M. G, P. Naik, Experimental Evaluation of Specific Heat Carrying Capacity of Fly-Ash Reinforced Aluminium 6061 Composite, Int. Res. J. Eng. Technol. (IRJET), India, 2015.

[49] J. Fujino, T. Honda, Measurement of the specific heat of plastic waste/fly ash composite material using differential scanning calorimetry, Int. J. Thermophys. 30 (2009), https://doi.org/10.1007/s10765-009-0575-5.

[50] B. D'Aguanno, M. Karthik, A.N. Grace, A. Floris, Thermostatic properties of nitrate molten salts and their solar and eutectic mixtures, Sci. Rep. 8 (2018), https://doi.org/10.1038/s41598-018-28641-1.

[51] S. Engelmann, R. Hentschke, Specific heat capacity enhancement studied in silica doped potassium nitrate via molecular dynamics simulation, Sci. Rep. 9 (2019) 7606, https://doi.org/10.1038/s41598-019-44132-3.

[52] A. Bonk, M. Braun, T. Bauer, Phase diagram, thermodynamic properties and long-term isothermal stability of quaternary molten nitrate salts for thermal energy storage, Sol. Energy 231 (2022), https://doi.org/10.1016/j.solener.2021.12.020.

[53] A. Anagnostopoulos, A. Alexiadis, Y. Ding, Molecular dynamics simulation of solar salt (NaNO3-KNO3) mixtures, Sol. Energy Mater. Sol. Cells 200 (2019) 109897, https://doi.org/10.1016/j.solmat.2019.04.019.

[54] A. Anagnostopoulos, A. Alexiadis, Y. Ding, Simplified force field for molecular dynamics simulations of amorphous SiO_2 for solar applications, Int. J. Therm. Sci. 160 (2021), https://doi.org/10.1016/j.ijthermalsci.2020.106647.
[55] A. Anagnostopoulos, A. Alexiadis, Y. Ding, Simplified force field for molecular dynamics simulations of amorphous SiO2 for solar applications, Int. J. Therm. Sci. 160 (2021) 106647, https://doi.org/10.1016/j.ijthermalsci.2020.106647.
[56] J.T. Cieśliński, S. Smolen, D. Sawicka, Effect of temperature and nanoparticle concentration on free convective heat transfer of nanofluids, Energies 14 (2021), https://doi.org/10.3390/en14123566.
[57] K. Khanafer, K. Vafai, A critical synthesis of thermophysical characteristics of nanofluids, Int. J. Heat Mass Transf. 54 (2011), https://doi.org/10.1016/j.ijheatmasstransfer.2011.04.048.
[58] Y. Xiong, X. Tian, X. Li, J. Ren, Q. Xu, Y. Wu, Y. Ding, Effects of expanded graphite on NaNO3/semi-coke ash shape-stable phase change composites for thermal energy storage, J. Energy Storage 72 (2023), https://doi.org/10.1016/j.est.2023.108648.
[59] Y. Xiong, C. Song, J. Ren, Y. Jin, B. Nie, Q. Xu, Y. Wu, C. Li, H. Li, Y. Ding, Sludge-incinerated ash based shape-stable phase change composites for heavy metal fixation and building thermal energy storage, Process Saf. Environ. Prot. 162 (2022), https://doi.org/10.1016/j.psep.2022.04.004.
[60] F. Jiang, Z. Ge, X. Ling, D. Cang, L. Zhang, Y. Ding, Improved thermophysical properties of shape-stabilized NaNO3 using a modified diatomite-based porous ceramic for solar thermal energy storage, Renew. Energy 179 (2021) 327–338, https://doi.org/10.1016/j.renene.2021.07.023.
[61] G. Xu, G. Leng, C. Yang, Y. Qin, Y. Wu, H. Chen, L. Cong, Y. Ding, Sodium nitrate – diatomite composite materials for thermal energy storage, Sol. Energy 146 (2017) 494–502, https://doi.org/10.1016/J.SOLENER.2017.03.003.
[62] A. Anagnostopoulos, M. Elena Navarro, S. Sharma, A. Ahmad, Y. Maksum, Y. Ding, From waste to value: utilising waste foundry sand in thermal energy storage as a matrix material in composites, Sol. Energy 268 (2024) 112294, https://doi.org/10.1016/J.SOLENER.2023.112294.